Research Article Vol. 3, No. 7 / 15 Jul 2024 / Optics Continuum 1051
OPTICS CONTINUUM

Pulse front distortions in focused spatially chirped beams

E. C. NELSON,* K. D. CHESNUT, T. REUTERSHAN, H. H. EFFARAH, K. J. CHARBONNET, AND C. P. J. BARTY

Department of Physics and Astronomy, University of California, Irvine, CA 92697, USA
*ecnelson@uci.edu

Abstract: A numerical analysis of spatially chirped beams produced by single-pass grating pairs is presented. It is shown that focused pulse structures can deviate significantly relative to standard linear spatial chirp approximations depending upon the pulse bandwidth, the angle of incidence, and groove density of the gratings used.

1. Introduction

The use and focusing of chirped beams was first proposed in 2004 as a route to produce ultra-high peak power laser pulses in a technique known as chirped beam amplification [1]. This concept, which is the spatial analog to chirped pulse amplification [2] (CPA), involves dispersing the spectral content of a pulse in a transverse spatial dimension to reduce its local intensity and thus avoid damage in amplifiers and final optics [3,4]. Focusing a chirped beam simultaneously reduces the spatial and temporal extent of the pulse in a technique that is commonly referred to as simultaneous spatial and temporal focusing (SSTF) [5,6]. The most frequently employed approach to SSTF is through the one-dimensional spatial chirp of a Gaussian beam profile generated with a grating pair. As an ultrashort pulse travels through the grating pair, its spectral components are spatially separated in one dimension, necessarily reducing the pulse's local spectral content and increasing the pulse's local pulse duration. As the beam focuses, the spectral components gradually spatially overlap until the pulse reaches both its minimum spatial width and its transform limited pulse duration at the focus. This leads to a pulse front tilt (PFT) whose orientation is a function of the magnitude of beam chirp and the f-number of the focusing system. SSTF has been used in multiphoton microscopy [7–9], micromachining, [10–12] and structured 3D printing [13].

Recently, focal spots with PFT have been studied in high intensity laser plasma experiments for electron acceleration where tuning the angle of the PFT enables electron steering [14,15] and target normal sheath acceleration (TNSA) schemes for improved maximum electron energies in TNSA target interactions [16]. Next-generation high-intensity lasers are potentially reaching the ultra-broadband spectral regime, with temporal pulse widths near 10 femtoseconds [17–19], where the study of space-time couplings, such as PFT, are relevant [20]. These lasers could be used for advanced acceleration schemes based on chirped beams and SSTF interactions for studying novel laser-matter interactions, including traveling wave excitation for soft x-ray amplification [21,22]. Additionally, SSTF systems can be used as part of a post-amplification pulse compression scheme [23].

Generating a high-peak-intensity PFT focal spot with the SSTF technique requires the use of a grating pair to spatially chirp the beam. Gratings impart a nonlinear spatial chirp across the bandwidth of the pulse, especially at near-infrared frequencies. In this work, we argue that for large-bandwidth pulses this grating-induced nonlinearity needs to be considered, as the linear approximation typically used in studying spatial chirp becomes significantly inaccurate. Careful choice of the gratings used to generate the spatial chirp is important because groove density and angle of incidence (AOI) affect the degree of nonlinearity, which in turn changes the

#526043 https://doi.org/10.1364/OPTCON.526043
Journal © 2024 Received 15 Apr 2024; revised 21 May 2024; accepted 4 Jun 2024; published 27 Jun 2024

OPTICS CONTINUUM

space-time structure as the pulse propagates through the focus. The nonlinearity also imparts a pulse front curvature (PFC) and varies the intensity localization, necessarily changing the fundamental interaction of the focusing laser pulse with matter. This manuscript aims to simulate and describe the characteristics of a chirped beam from spatial chirp configurations generated using different grating pairs and provide an open-source Python3 simulation package [24] to aid in the exploration of arbitrary, short pulse, space-time light fields propagating through a focal volume. All simulations were done using linear Fourier propagation techniques utilizing scalar diffraction theory, concentrating on propagation in the linear regime to provide insight into the space-time structure of these pulses.

2. Methods

2.1. System design

A typical SSTF system consists of a grating pair that spreads the frequency components of a laser pulse in 1D, shown in Fig. 1. To have a transform limited pulse at the focus, a positive temporal pre-chirp must be imparted on the pulse to compensate for the temporal group delay dispersion from the grating pair. This is readily achieved, as the two gratings in Fig. 1 act as half of a Treacy compressor [25], whose induced temporal chirp on the incident laser pulse can be perfectly compensated with an upstream Martinez stretcher [26,27]. To have temporal compensation with only half of a compressor, the separation between the gratings must be doubled from the values defined for a 4-grating or double-pass 2-grating arrangement. The amount of chirp in this system can be defined by the beam aspect ratio (BAR) of the chirped beam, where

$$\mathrm{BAR} = \frac{D_{\mathrm{chirp}}}{D_{\mathrm{in}}}, \tag{1}$$

The initial beam diameter is D_{in} and the effective beam diameter in the chirped dimension is D_{chirp}. This value can be tuned by varying the grating separation and changing the temporal pre-compensation.

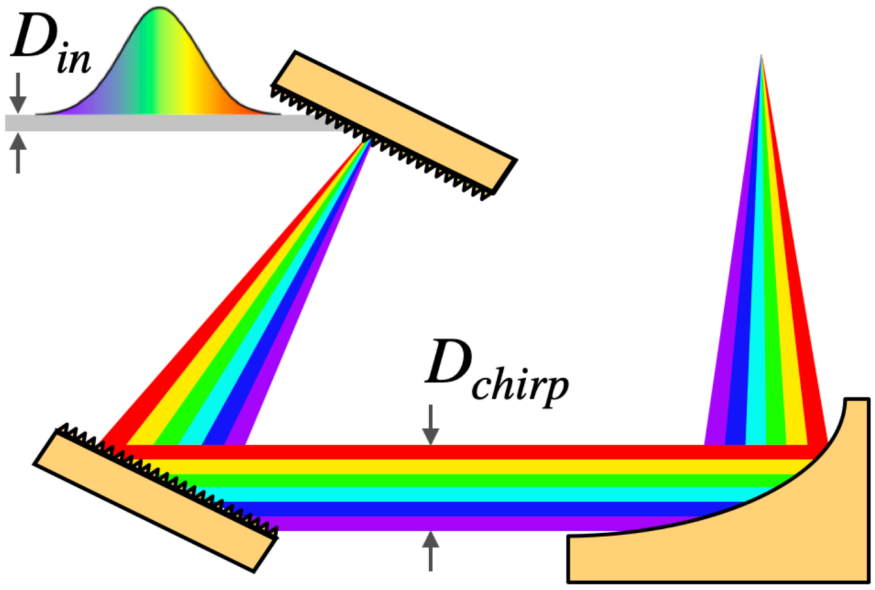

Fig. 1. A two grating compressor oriented to create simultaneous spatial and temporal focusing of a pulse.

OPTICS CONTINUUM

2.2. Simulation model

We developed an open source linear Fourier optics code in Python3 to simulate a user-defined electric field propagating through an ideal lens and free space. The electric field can be visualized at any position throughout the focal volume to observe the effects different system parameters have on the pulse profile at and near the focus. Any spatial profile and spectrum can be modeled and propagated. We focus on a Gaussian beam in space and frequency for its simplicity and ease of interpolating results. An initial electric field that is Gaussian in space and spectrum is defined before the focusing optic of the form [6]:

$$E(x_1, y_1, z = 0, \omega) = E_0 E(\omega) E(x_1, y_1) = E_0 \exp\left[-\frac{(\omega - \omega_0)^2}{\Delta\omega^2}\right] \exp\left(-\frac{x_1^2 + y_1^2}{w_{\text{in}}^2}\right), \tag{2}$$

where $\Delta\omega$ is the $1/e^2$ half-width bandwidth of the spectrum, ω_0 is the center frequency, and $w_{\text{in}} = D_{\text{in}}/2$ is the $1/e^2$ beam radius of the field intensity. The simulations presented here are based on a typical Ti:Sapphire laser system with a center wavelength of 800 nm, a beam radius of 0.5 mm, a focal spot size radius of 50.5 μm, and a full width at half max bandwidth of 100 nm, resulting in a transform-limited pulse width of $\sim$ 9.4 fs. In the simulations, the initial electric field is defined on a square numeric grid with spatial lengths $L_{1,x} \times L_{1,y}$ and spacing Δx_1 and Δy_1, whose values depend on the initial conditions of the model, such as beam diameter, chirped beam diameter, and focal length.

The initial spatial electric field used to describe a linearly polarized beam with 1D linear spatial chirp in the x-direction is typically expressed as [6,8,33–35]:

$$E(x_1, y_1) = \exp\left\{-\frac{[x_1 \pm \alpha(\omega - \omega_0)]^2 + y_1^2}{w_{\text{in}}^2}\right\}, \tag{3}$$

The chirp rate, α, which is the amount that each frequency component is separated from the previous, is assumed constant, resulting in a linear separation between frequency components. This approximation is valid only for pulses with small bandwidths based on a Taylor expansion analysis [34].

In practice, the spatial chirp from a grating pair is nonlinear in frequency and is derived from the grating equation, where the spatial dependence on frequency is:

$$x_{\text{chirp}}(\omega) = L \tan\left[\sin^{-1}\left(\frac{-2\pi mcd}{\omega} - \sin\theta_i\right)\right], \tag{4}$$

and the new chirp rate becomes:

$$\alpha(\omega) = \frac{dx_{\text{chirp}}(\omega)}{d\omega}, \tag{5}$$

where L is the separation between the grating pair, d is the groove density, m is the diffraction order, c is the speed of light, and θ_i is the angle of incidence on the grating.

Seen in Fig. 2, the spatial chirp generated by a grating pair is increasingly nonlinear for lower frequencies, so the linear chirp approximation breaks down and the full calculation must be considered. As smaller angles of incidence are used, the nonlinearity increases. We refer to this kind of chirp as nonlinear chirp. The definition of the electric field now has the form:

$$E(x_1, y_1, \omega) = \exp\left(-\frac{\left[x_1 - x_{\text{chirp}}(\omega)\right]^2 + y_1^2}{w_{\text{in}}^2}\right). \tag{6}$$

From here, the pulse can then be propagated through an ideal lens and to the focal plane of the system using the Fraunhofer propagation operator acting on the field [36,37]:

$$E(x_2, y_2, z = f, \omega) = \frac{\omega}{i2\pi cf} \exp\left[\frac{i\omega}{2cf}\left(x_2^2 + y_2^2\right)\right] \times FFT[E(x_1, y_1, z = 0, \omega)]\Delta x_1 \Delta y_1, \tag{7}$$

OPTICS CONTINUUM

where f is the focal distance of the lens and x_2 and y_2 are the x and y coordinates of the focal plane. The modified focal plane grid dimensions are $L_{2,x} = \lambda f/\Delta x_1$ and $L_{2,y} = \lambda f/\Delta y_1$ with grid spacing $\Delta x_2 = \lambda f/L_{1,x}$ and $\Delta y_2 = \lambda f/L_{1,y}$. Since the electric fields are polychromatic, each frequency component's focal plane dimensions are calculated and scaled to the plane of the center frequency, ω_0.

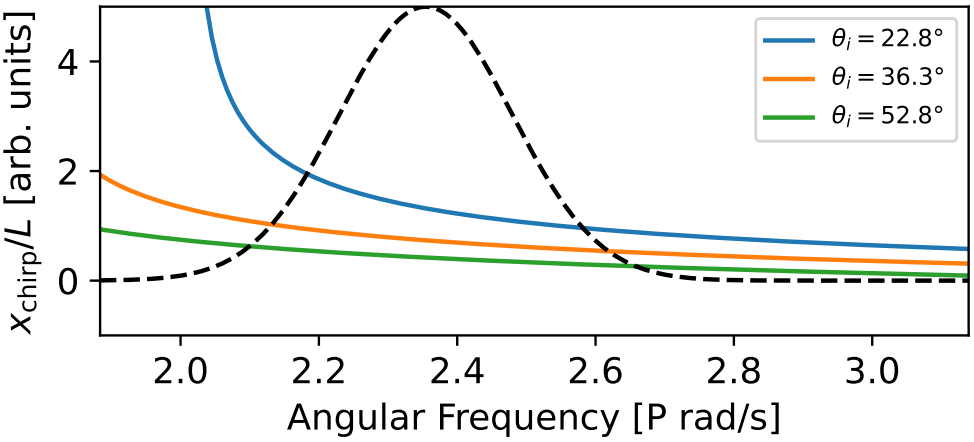

Fig. 2. Normalized spatial chirp as a function of frequency is shown for three cases of AOI, θ_i, for a 1480 lines/mm grating pair used in a Ti:Sapphire CPA system [28–32]. The spectrum of the 9.4 fs, 800 nm Ti:Sapphire laser used in this paper is shown as a dashed line.

With this result, the field at the focus can be visualized. The field can then be propagated within the focal region using the Angular Spectrum of Plane Waves (ASPW) operator [37]:

$$E(x_2, y_2, z = f + \Delta z, \omega) = FFT^{-1}[FFT[E(x_2, y_2, z = f, \omega)] \exp(ik_z \Delta z)], \tag{8}$$

with $k_z = \sqrt{(\omega/c)^2 - (2\pi f_x)^2 - (2\pi f_y)^2}$, and where f_x and f_y are the Fourier transform sample frequencies of x_2 and y_2.

The temporal distribution can be calculated at any position by taking a Fourier transform with respect to time of this field. Two different Fourier propagators are used to relax computational requirements in different propagation regimes that have different sampling conditions to ensure accurate results.

3. Results

For all the simulations, ideal optics are assumed so that there is 100% efficiency into the $m = -1$ diffraction order of the gratings and the f-number of the system is set so there is paraxial focusing. Additionally, only the chirped spatial dimension (x) was simulated to allow for increased resolution and reduce computational cost. Excluding the unchirped spatial dimension (y) from the simulations is valid when considering large amounts of spatial chirp due to a significantly reduced contribution to intensity localization at the focus. For each grating arrangement simulated, perfect temporal chirp compensation is assumed. This allows a clearer interpretation of the influence of nonlinear spatial chirp.

The initial chirp can be represented in (x, ω) space shown in Fig. 3. Figure 3(a) represents a linear chirp along the x-dimension, where a linear dependence can be seen in the spatial position of the frequency content. The higher frequencies are chirped in the positive x-direction and the lower frequencies in the negative x-direction. The frequencies are chirped symmetrically about the center frequency, ω_0. Figures 3(b)-3(d) show an equivalent chirp modeled with the grating

OPTICS CONTINUUM

equation (Eq. (6)) for a 1480 lines/mm grating pair with varying angles of incidence. The spatial extent of the nonlinear chirps was chosen so that the angle the PFT makes with respect to the propagation axis at the focus is same for all cases. This was achieved by varying the grating separation. Each configuration was set so that the PFT angle (θ_{PFT}) was 45°. For the linear chirp, this corresponds to a BAR ≈ 21, calculated from the relationship [38]:

$$\tan\left(\theta_{\mathrm{PFT}}\right) = \frac{w_{\mathrm{in}}\omega_0\sqrt{\mathrm{BAR}^2 - 1}}{f\Delta\omega}, \tag{9}$$

with θ_{PFT} set to 45°. Due to the higher diffraction angle of the lower frequencies, there is more spectral content around the higher frequencies. This results in an asymmetry in the spatial extent of the beam. Even though the PFT at the focus was kept constant, the spatial and temporal representations of the field at the input plane of the simulations are different. The grating pair introduces the same directional dependence of chirp along the x-dimension, but the lower frequencies experience a large nonlinearity in the chirp rate, shown in Fig. 2. Depending on the incidence angle used, the nonlinear dependence of the spatial chirp can be minimized. As AOI is increased, the spatial chirp becomes more linear.

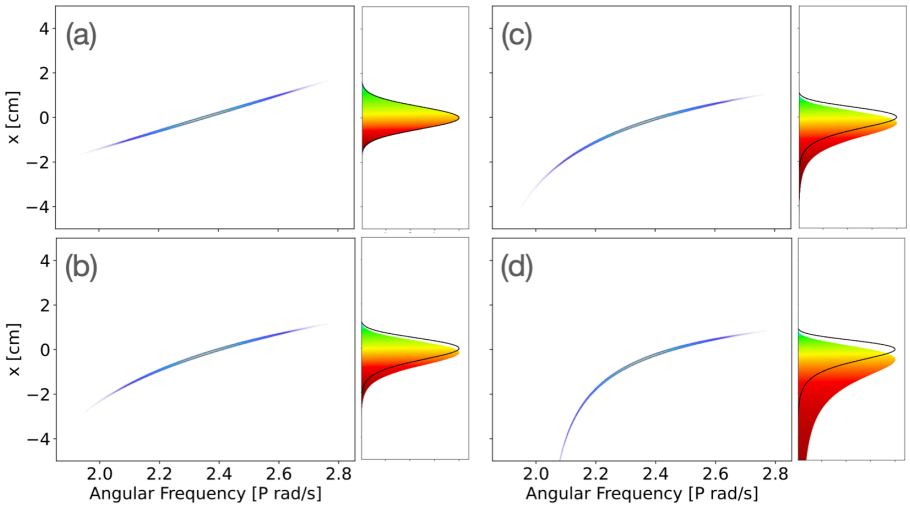

Fig. 3. Comparison of the initial transverse fields for both linear and nonlinear spatial chirps. The chirp is shown in the space-frequency domain and also as a lineout of the intensity along the x-dimension. The colored components show the spatial chirp in the space-frequency domain, where the longer wavelengths have been diffracted more than the shorter. The solid black line shows the spatial chirp after a Fourier transform into the space-time domain. Shows a (a) linear chirp and (b)-(d) nonlinear chirp generated with angles of incidence: 52.8°, 36.3°, and 22.8°, respectively.

To highlight the importance of considering the realistic chirp from a grating pair of an ultrashort pulse, the propagation of a linear chirp and equivalent nonlinear chirps are shown in Figs. 4 and 5. A grating pair with 1480 lines/mm at three typical incidence angles, 22.8°, 36.3°, and 52.8°, are simulated. These gratings and angles are used as common configurations (high dispersion, Littrow, and low dispersion, respectively) for Ti:Sapphire compressors with high efficiency and high damage thresholds [28–31]. Recent work is being conducted for this groove density on increasing supported bandwidths up to 400 nm [39]. Figure 4 shows four different pulses propagating in (x, t) space at various z-positions and Fig. 5 shows the same pulses propagating in (x, z) space at various times, highlighting the PFC differences. Both frames of reference are

OPTICS CONTINUUM

important for visualization. To see how the pulse interacts with a planar surface, in traveling wave excitation or dielectric laser acceleration for example, the (x, t) space at a z-position provides this information. The spatial dependence of the (x, z) space is relevant in electron acceleration where the gradient is proportional to the ponderomotive force. Figures 4(a) and 5(a) illustrate the space-time and spatial focusing, respectively, of a beam chirped linearly in frequency. The PFT in this type of pulse has been shown to accelerate electrons normal to the tilted pulse front and focus an electron bunch due to the concave PFC [14,15,38]. Figures 4(b)–4(d) and 5(b)–5(d) show the nonlinear spatial chirps.

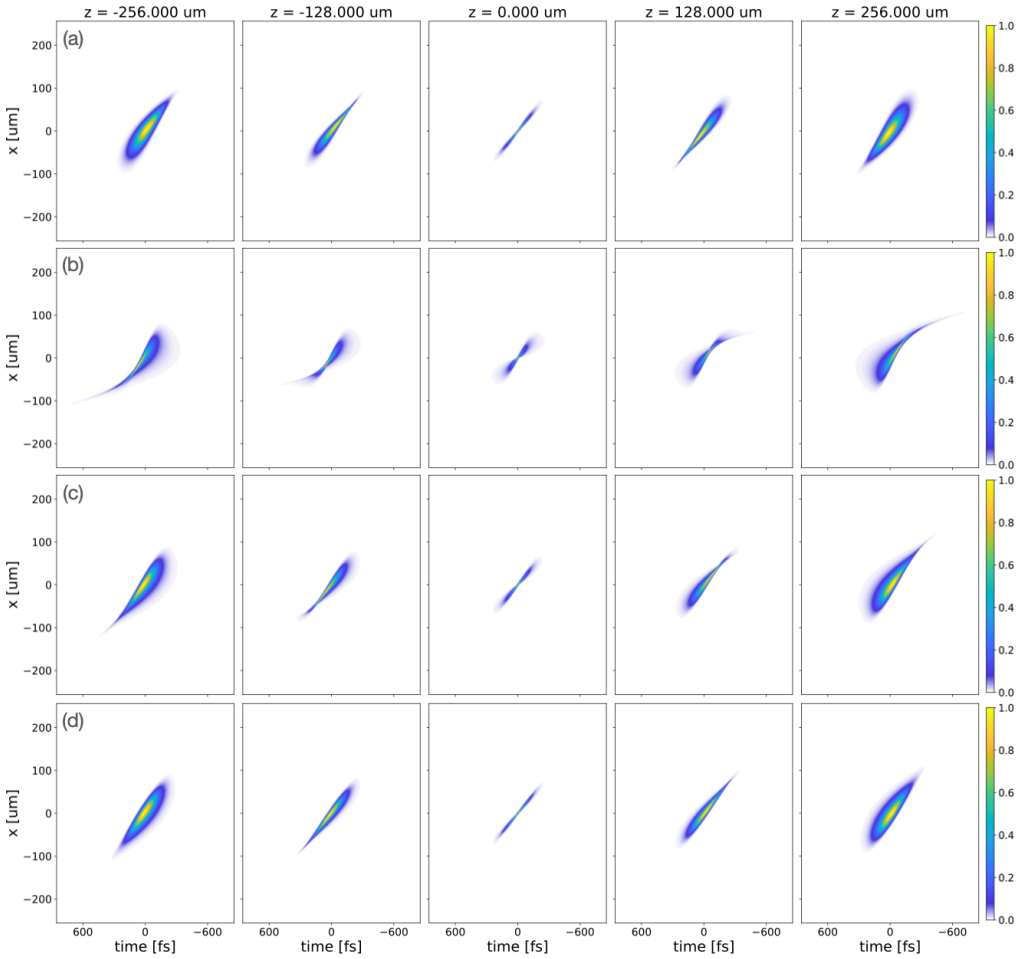

Fig. 4. Propagation of a focused spatially chirped beam with a PFT of 45° for a linear frequency chirp and nonlinear chirp represented in (x, t) space. The temporal representations of the propagation of a (a) linear chirp and (b)-(d) nonlinear chirps generated with 1480 lines/mm gratings and incidence angles of 22.8°, 36.3°, and 52.8°, respectively, are shown.

Comparing the focal position (t = 0 fs and z = 0 μm) of both the linear and nonlinear chirps, the outside edges of the pulse structures are different, leading to various amounts of concave PFC across the cases. The chirp generated with the lower AOI has more noticeable curvature, whereas larger AOI chirps minimized the amount of variation in the pulse front. The chirp generated with the largest incidence angle had the biggest reduction in PFC at the focus, even less than the linear frequency approximation. Within the focal volume, as the pulse propagates to the focal plane,

OPTICS CONTINUUM

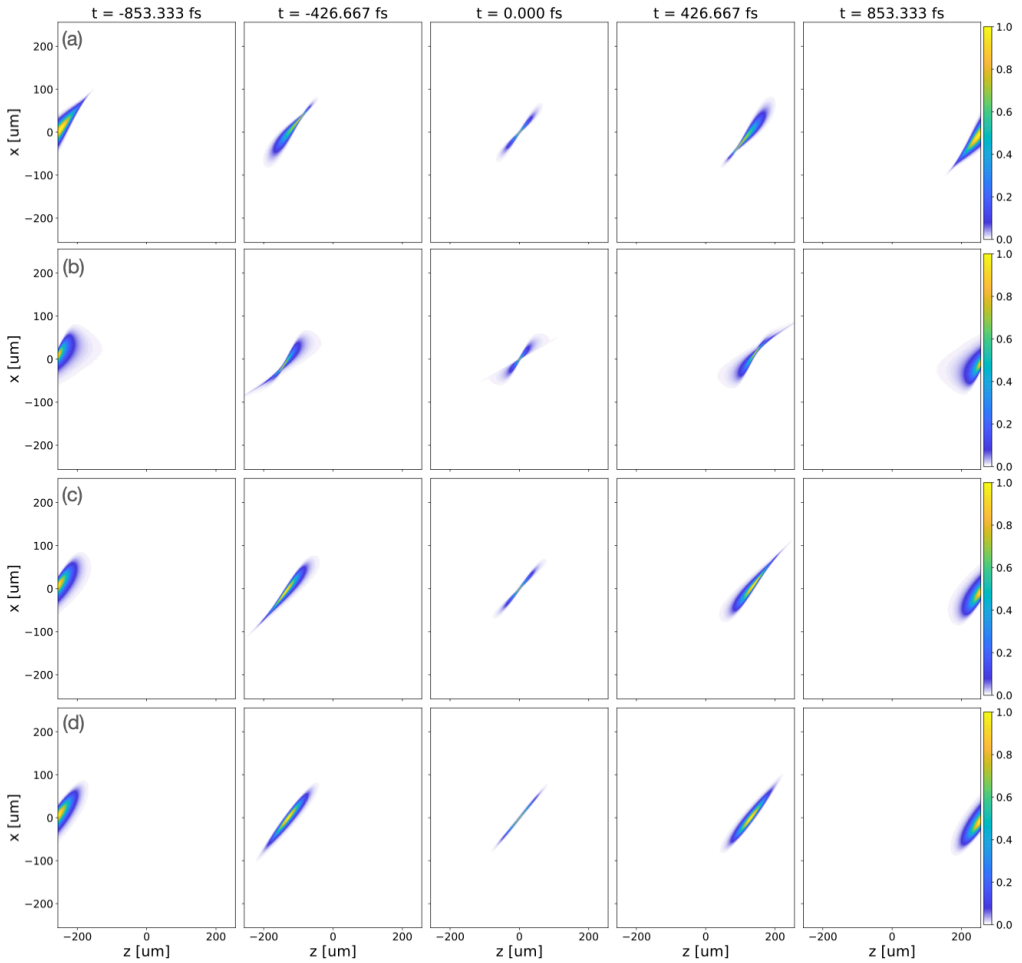

Fig. 5. Propagation of a focused spatially chirped beam with a PFT of 45° for a linear frequency chirp and nonlinear chirp represented in (x, z) space. The spatial representation of the propagation of a (a) linear chirp and (b)-(d) nonlinear chirps generated with 1480 lines/mm gratings and incidence angles of 22.8°, 36°, and 52.8°, respectively, are shown.

there are also significant differences in the pulse structure. In the leading frames, the curvature of the pulse front is flipped between the linear frequency approximation and the nonlinear chirp cases.

While the orientation of arrival time in the transverse extent of the pulse is the same across all cases (namely, the part of the beam in the positive x-direction leads in time), the sweeping of the smallest spatial extent across the transverse chirped dimension varies between the linear and nonlinear chirped cases. In the linear frequency approximation, the pulse sweeps from positive to negative x, whereas this direction is inverted in the realistic simulation of the grating pair. This property results in the peak intensity of the beam deviating from on-axis. Figure 6 shows the location of the peak transverse intensity along with the peak intensity. The propagation effects for the linear approximation, 22.8°, 36.3°, and 52.8°cases are shown in Visualization 1, Visualization 2, Visualization 3, and Visualization 4, respectively. The simulations were limited to a 1-μm resolution along the transverse dimension to reduce computation time. In all the cases, the peak intensity as the beam focuses is not on-axis ($x = 0, y = 0$) but varies with the propagation.

OPTICS CONTINUUM

This is contrary to the focusing of an unchirped beam where the peak intensity stays on-axis while propagating through a focus [40]. The peak intensity is more localized both longitudinally and transversely in the high AOI grating configuration (Fig. 6(d)), and progressively increases in transverse deviation for smaller angles of incidence. The linear frequency chirp approximation in Fig. 6(a), has the largest translation in the transverse dimension, and the lowest incidence angle of 22.8° (Fig. 6(b)) has the largest longitudinal extent.

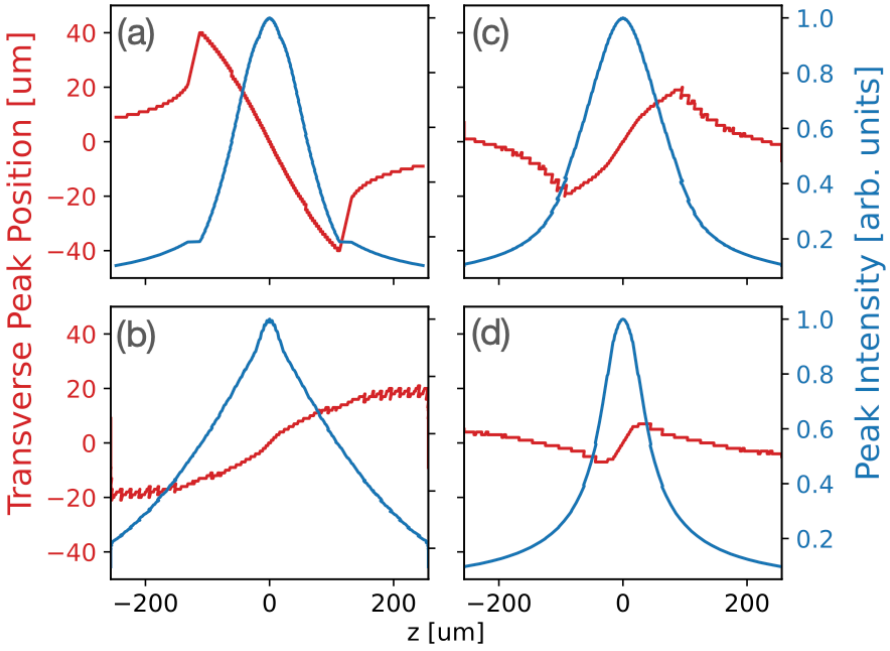

Fig. 6. Transverse peak intensity position (red) and longitudinal intensity profile (blue) for the linear and nonlinear chirps. The (a) linear chirp and (b)-(d) nonlinear chirps for AOIs of 22.8°, 36.3°, and 52.8°, respectively, are shown.

Figure 7 compares the dependence of the spatial chirp as a function of frequency and wavelength for different angles of incidence for a PFT of 45°. In Fig. 7(a), as the angle increases, the nonlinearity is reduced but never approaches linear. Converting from frequency to wavelength

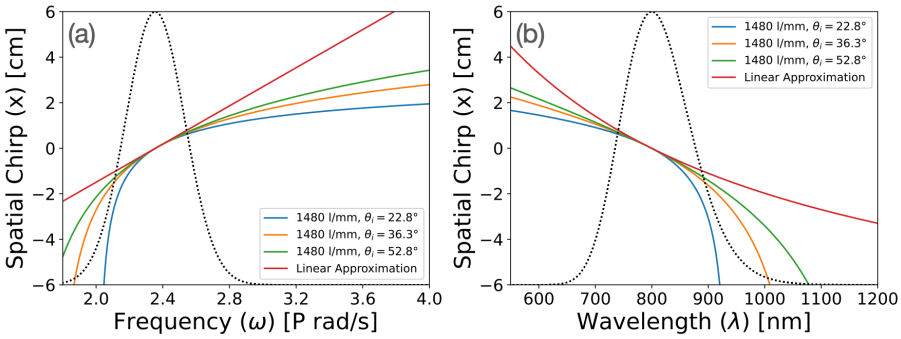

Fig. 7. Spatial chirp as defined by Eq. (6) for a PFT of 45° with varying angles of incidence. The dotted line overlays the spectrum for the simulated Gaussian pulse. The spatial chirp as a function of (a) frequency and as a function of (b) wavelength.

OPTICS CONTINUUM

(Fig. 7(b)) illuminates the difference in pulse front structure of the cases shown in Figs. 4 and 5. In this representation, as the angle decreases, the spatial chirp approaches a linear trend across the bandwidth, whereas the linear frequency chirp approximation has a nonlinear trend with the opposite concavity than that from the grating pair. The grating cases are concave down, and the linear chirp is concave up. These lead to different pulse front orientations and pulse front curvatures seen in Figs. 4 and 5.

4. Conclusion

With the increased interest in spatio-temporal control of ultrashort pulses for high intensity laser applications, such as SSTF, it is important to understand how these pulses evolve as they propagate through the focus. For large bandwidth pulses, the linear approximation of spatial chirp from a grating pair breaks down and provides an unrealistic model for focused spatially chirped beams. The effect of the spatial chirp nonlinearity introduced by the grating pair can change the orientation and severity of the pulse front curvature within the focal volume and, therefore, change its interaction with matter. By choosing an appropriate angle of incidence, the characteristics of the focal volume can be tuned for a given PFT. The code developed allows the ability to propagate an arbitrarily defined electric field through a focus which enables the study of higher order chirp or more complex pulse structures.

Disclosures. The authors declare no conflicts of interest.

Data availability. Data underlying the results presented in this paper along with the code used to generate the figures are available in Ref. [24].

References

1. C. P. J. Barty, "Optical chirped beam amplification and propagation," U.S. patent 6,804,045B2 (12 October 2004).
2. D. Strickland and G. Mourou, "Compression of amplified chirped optical pulses," Opt. Commun. **55**(6), 447–449 (1985).
3. C. P. J. Barty, "The nexawatt: a strategy for exawatt peak power lasers based on NIF and NIF-like beam lines," J. Phys.: Conf. Ser. **717**, 012086 (2016).
4. K. D. Chesnut and C. P. J. Barty, "Ideal spatio-temporal pulse distribution for exawatt-scale lasers based on simultaneous chirped beam and chirped pulse amplification," Opt. Express **31**(4), 5687–5698 (2023).
5. G. Zhu, J. v. Howe, M. Durst, *et al.*, "Simultaneous spatial and temporal focusing of femtosecond pulses," Opt. Express **13**(6), 2153–2159 (2005).
6. C. G. Durfee, M. Greco, E. Block, *et al.*, "Intuitive analysis of space-time focusing with double-ABCD calculation," Opt. Express **20**(13), 14244–14259 (2012).
7. D. Oron, E. Tal, and Y. Silberberg, "Scanningless depth-resolved microscopy," Opt. Express **13**(5), 1468–1476 (2005).
8. M. E. Durst, G. Zhu, and C. Xu, "Simultaneous spatial and temporal focusing for axial scanning," Opt. Express **14**(25), 12243–12254 (2006).
9. E. Papagiakoumou, E. Ronzitti, and V. Emiliani, "Scanless two-photon excitation with temporal focusing," Nat. Methods **17**(6), 571–581 (2020).
10. D. N. Vitek, E. Block, Y. Bellouard, *et al.*, "Spatio-temporally focused femtosecond laser pulses for nonreciprocal writing in optically transparent materials," Opt. Express **18**(24), 24673–24678 (2010).
11. R. Kammel, R. Ackermann, J. Thomas, *et al.*, "Enhancing precision in fs-laser material processing by simultaneous spatial and temporal focusing," Light: Sci. Appl. **3**(5), e169 (2014).
12. A. Patel, Y. Svirko, C. Durfee, *et al.*, "Direct writing with tilted-front femtosecond pulses," Sci. Rep. **7**(1), 12928 (2017).
13. Y. Tan, W. Chu, P. Wang, *et al.*, "High-throughput multi-resolution three dimensional laser printing," Phys. Scr. **94**(1), 015501 (2019).
14. A. M. Wilhelm and C. G. Durfee, "Tilted snowplow ponderomotive electron acceleration with spatio-temporally shaped ultrafast laser pulses," Front. Phys. (2019).
15. P. Hunt, A. Wilhelm, and D. Adams, "Ponderomotive snowplow electron acceleration with high energy tilted ultrafast laser pulses (preprint)," Research Square, rs.3.rs-4177060/v1 (2024).
16. E. S. Grace, B. Z. Djordjevic, Z. Guang, *et al.*, "Single-shot measurements of pulse-front tilt in intense ps laser pulses and its effect on accelerated electron and ion beam characteristics (invited)," Rev. Sci. Instrum. **93**(12), 123508 (2022).
17. Z. Li, Y. Kato, and J. Kawanaka, "Simulating an ultra-broadband concept for exawatt-class lasers," Sci. Rep. **11**(1), 151 (2021).

OPTICS CONTINUUM

18. W. Liang, S. Du, R. Chen, *et al.*, "Viability verification of asymmetric four-grating compressor in sel-100 PW frontend," Opt. Commun. **557**, 130317 (2024).
19. M. Aléonard, M. Altarelli, and P. Antici, *WHITEBOOK ELI - Extreme Light Infrastructure; Science and Technology with Ultra-Intense Lasers* (Andreas Thoss, 2011).
20. A. Jeandet, S. W. Jolly, A. Borot, *et al.*, "Survey of spatio-temporal couplings throughout high-power ultrashort lasers," Opt. Express **30**(3), 3262–3288 (2022).
21. Z. Bor, S. Szatmári, and A. Müller, "Picosecond pulse shortening by travelling wave amplified spontaneous emission," Appl. Phys. B **32**(3), 101–104 (1983).
22. C. P. J. Barty, D. A. King, G. Y. Yin, *et al.*, "12.8-ev laser in neutral cesium," Phys. Rev. Lett. **61**(19), 2201–2204 (1988).
23. J. Liu, X. Shen, S. Du, *et al.*, "Multistep pulse compressor for 10s to 100s PW lasers," Opt. Express **29**(11), 17140–17158 (2021).
24. E. C. Nelson, "SSTF-nonlinear.tar.gz," figshare (2024) , https://doi.org/10.6084/m9.figshare.25869163.
25. E. Treacy, "Optical pulse compression with d0iffraction gratings," IEEE J. Quantum Electron. **5**(9), 454–458 (1969).
26. O. Martinez, "3000 times grating compressor with positive group velocity dispersion: application to fiber compensation in 1.3-1.6 μm region," IEEE J. Quantum Electron. **23**(1), 59–64 (1987).
27. M. Pessot, P. Maine, and G. Mourou, "1000 times expansion/compression of optical pulses for chirped pulse amplification," Opt. Commun. **62**(6), 419–421 (1987).
28. T. J. Yu, S. K. Lee, J. H. Sung, *et al.*, "Generation of high-contrast, 30 fs, 1.5 PW laser pulses from chirped-pulse amplification Ti:sapphire laser," Opt. Express **20**(10), 10807–10815 (2012).
29. V. Aleksandrov, G. Bleotu, L. Caratas, *et al.*, "Upgrading design of a multi-TW femtosecond laser," Romanian Reports in Physics (2020).
30. Y. Chu, Z. Gan, X. Liang, *et al.*, "High-energy large-aperture ti:sapphire amplifier for 5 PW laser pulses," Opt. Lett. **40**(21), 5011 (2015).
31. C. M. Werle, C. Braun, T. Eichner, *et al.*, "Out-of-plane multilayer-dielectric-grating compressor for ultrafast ti:sapphire pulses," Opt. Express **31**(23), 37437–37451 (2023).
32. F. Lureau, G. Matras, O. Chalus, *et al.*, "High-energy hybrid femtosecond laser system demonstrating 2 × 10 pw capability," High Power Laser Sci. Eng. **8**, e43 (2020).
33. R. Kammel, K. Bergner, and J. Thomas, "Simultaneous spatial and temporal focusing: a route towards confined nonlinear materials processing," Proc. SPIE **9736**, 97360T (2016).
34. F. He, Y. Cheng, J. Lin, *et al.*, "Independent control of aspect ratios in the axial and lateral cross sections of a focal spot for three-dimensional femtosecond laser micromachining," New J. Phys. **13**(8), 083014 (2011).
35. S. Zhang, D. Asoubar, R. Kammel, *et al.*, "Analysis of pulse front tilt in simultaneous spatial and temporal focusing," J. Opt. Soc. Am. A **31**(11), 2437–2446 (2014).
36. D. G. Voelz, *Computational Fourier Optics: A MATLAB Tutorial* (SPIE, 2011).
37. J. W. Goodman, *Introduction to Fourier Optics* (McGraw-Hill, 1988).
38. A. M. Wilhelm, "Tilted snowplow electron acceleration with simultaneously spatially and temporally focused laser pulses," Ph.D. dissertation (Colorado School of Mines, 2021).
39. Y. Han, Z. Li, Y. Zhang, *et al.*, "400nm ultra-broadband gratings for near-single-cycle 100 petawatt lasers," Nat. Commun. **14**(1), 3632 (2023).
40. A. E. Siegman, *Lasers* (University Science Books, 1986).